22

Wave Propagation and Dynamic Fracture in Laser Shock-Loaded Solid Materials

Thibaut De Rességuier[1], Jean-Paul Cuq-Lelandais[1], Michel Boustie[1], Emilien Lescoute[1] and Laurent Berthe[2]
[1]*Laboratoire de Combustion et de Détonique (CNRS, ENSMA)*
[2]*Laboratoire Procédés et Ingénierie en Mécanique et Matériaux (Arts et Métiers, ParisTech)*
France

1. Introduction

Shock wave loading of solid materials results in specific damage processes at high strain rates. The most widely studied of these processes is probably spall fracture (e.g. Antoun et al., 2002, and references therein), which arises from tensile stresses generated by the interaction of release waves within the material upon reflection of a compressive pulse from a free surface or from an interface with a layer of lower acoustic impedance. If such tensile stresses exceed the dynamic strength of the material, they cause the nucleation and growth of micro-voids or micro-cracks which may eventually coalesce to form a macroscopic fracture and lead to the ejection of one or several fragments (spalled layers) from the sample. Spall damage and wave propagation are tightly coupled. On one hand, the creation of new free surfaces accompanying damage development induces stress relaxation which gives rise to recompression waves. Such waves can be detected in time-resolved velocity (Antoun et al., 2002; Tollier et al., 1998) or piezoelectric (De Rességuier et al., 1997) measurements, and their analysis provides very rich data on the fracture process (location, time and tensile stress at damage initiation, rate of the damage growth, thickness of the spalled layer…). On the other hand, spall fracture results from wave interaction, so that post-test observations of the residual damage in recovered samples (location, sizes and shapes of the damages zones, fracture surface morphology…) may provide key information on the propagation of compression and release waves prior to failure. In this chapter, we illustrate this second, more original statement with experimental results obtained under laser driven shock loading. Intense irradiation of an absorbing target by a high power pulsed laser produces the vaporization of a thin layer of material, transformed into a plasma cloud, whose expansion toward the laser source induces by reaction a compressive pulse into the solid target. The main specificity of this technique is the very short time of pressure application (typically a few ns) compared to other shock generators such as plate impacts or explosive loading, where the duration of the pressure load is usually of µs-order. This difference makes laser shocks less destructive than those more conventional techniques, and favours sample recovery for post-shock analyses of residual damage.

In a first example, spall fracture observed in laser shock-loaded single crystal quartz provides very clear evidence of the strong effect of crystal anisotropy on stress wave

Source: Wave Propagation in Materials for Modern Applications, Book edited by: Andrey Petrin,
ISBN 978-953-7619-65-7, pp. 526, January 2010, INTECH, Croatia, downloaded from SCIYO.COM

propagation, which is confirmed and explained by three-dimensional (3D) numerical simulations. In a second application, laser shock-induced damage in aluminium samples of different aspect ratios reveals edge effects associated to highly 2D propagation of the stress waves. In a third case, the fracture surface morphology observed in iron samples spalled under laser shock loading is used to investigate a shock-induced phase transformation occurring in this metal and its influence on wave propagation.

2. Anisotropic wave propagation in laser shock-loaded single crystal quartz

The crystalline structure of α-quartz is schematically shown in Fig. 1. It is unchanged under a 180° rotation around the electrical axis x, or under a 120° rotation around the optical axis z. The y axis, usually called mechanical axis, completes the (x,y,z) Cartesian coordinates. To explore the dependence of the dynamic behaviour on the initial direction of shock application relatively to those crystallographic orientations, we have determined experimentally the directions of the mechanical (y) and optical (z) axes in our samples (originally cut normally to the x axis), using uniaxial birefringent properties of quartz. For normal incidence of light on x-cut quartz, extraordinary transmitted rays are polarised parallel to the optical axis z, whereas ordinary transmitted rays are polarised parallel to the y axis. Thus, when an x-cut crystal set between two crossed polarisers is rotated around the x axis, the incident light stops being transmitted as soon as either the y or the z axis of the crystal becomes parallel to the transmission axis of one of the polarisers. That way we determine two particular axes y or z, normal to each other. Finally, to distinguish between those two axes, we use the fact that for normal incidence on z-cut quartz, the intensity of the transmitted light does not depend on the crystal orientation between the crossed polarisers.

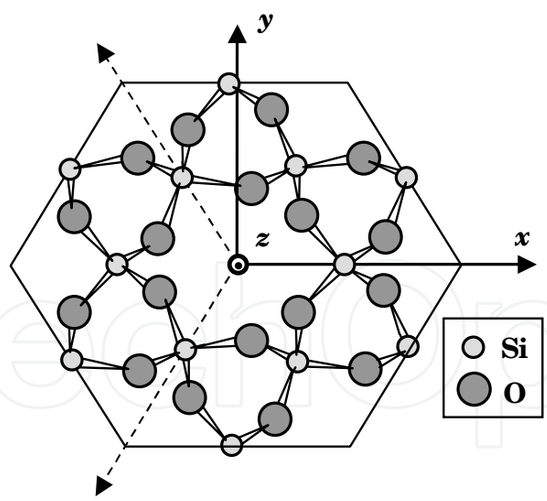

Fig. 1. Schematic view of the quartz structure, showing the electrical (x), mechanical (y) and optical (z) axes in the atomic arrangement of SiO_4 tetraedra.

The laser shock experiments have been performed in the *Laboratoire pour l'Utilisation des Lasers Intenses* (LULI, UMR #7605, Ecole Polytechnique, France). The samples are about 5 mm-thick, covered with a ~5 µm-thick gold coating. Shock loading is achieved by focussing a laser pulse of 1.06 µm-wavelength, ~2.2 ns-duration and ~90 J-energy onto a spot of diameter ranging from 1.2 to 4 mm, which leads to intensities of about 0.3 to 3.6 TW/ cm² (1

TW = 10^{12} W). The gold layer is ablated into a plasma cloud. Its expansion induces a short compressive pulse in the quartz sample, due to recoil action. Laser-matter interaction computations indicate that the corresponding loading pressure, which increases with laser intensity, ranges from about 10 to 80 GPa. After each shot, the recovered samples are examined, some are embedded in a resin, sectioned through a plane containing the laser axis, polished and observed in optical microscopy.

Fig. 2 shows a partial view of the free surface of a 5 mm-thick quartz sample recovered after a laser shock of 42 GPa (1.56 TW/ cm^2) applied onto a spot of diameter 1.6 mm in the opposite surface, along the *x* axis of the crystal (i.e. the irradiated surface was normal to the *x* axis). The gold coating has been removed from an elliptical region (dark area) much wider than the irradiated spot, and two cracks can be seen near both extremities of that zone. The dimensions of the ellipsoid are ~ 7.8 × 2.5 mm, the angle between its major axis and the *z* axis of the crystal is about 36°. Given the lateral dimensions of the samples (15 mm), this elliptical damage cannot be due to edge effects. Instead, it is likely to result from specifically orientated wave propagation due to the anisotropic structure of the crystal.

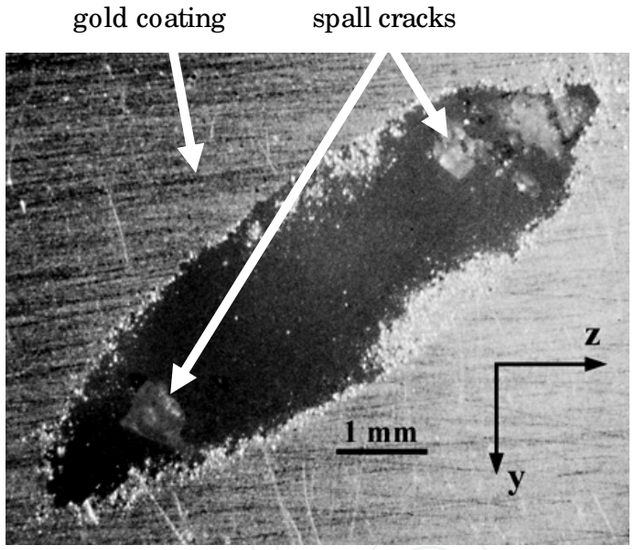

Fig. 2. Free surface of a 5 mm-thick quartz sample recovered after a laser shock of ~42 GPa applied onto a 1.6 mm-diameter spot in the opposite surface, along the *x* axis.

When the shock is applied along the *y* axis, the spalled zone near the free surface remains roughly circular, although slightly 'D'-shaped (Fig. 3a), but it is shifted in the *z* direction, about 1.6 mm away from the irradiated spot (while no damage was observed in the *–z* direction), as can be confirmed by a cross section along a *y-z* plane (Fig. 3b). That lateral shift, which has been observed in all similar shots, indicates an oblique propagation of the stress pulse when applied along the *y* axis. Finally, in all samples shocked along the *z* axis, a single, roughly circular spalled zone opposite to the irradiated spot can be observed (Fig. 4), like would be evidenced in a brittle, isotropic target such as a glass plate (De Rességuier & Cottet, 1995; Li et al., 1998).

To comfort our interpretation of the above observations as effects of quartz anisotropy, we have performed 3D Lagrangian computations with the explicit code *Radioss*. Due to the fast

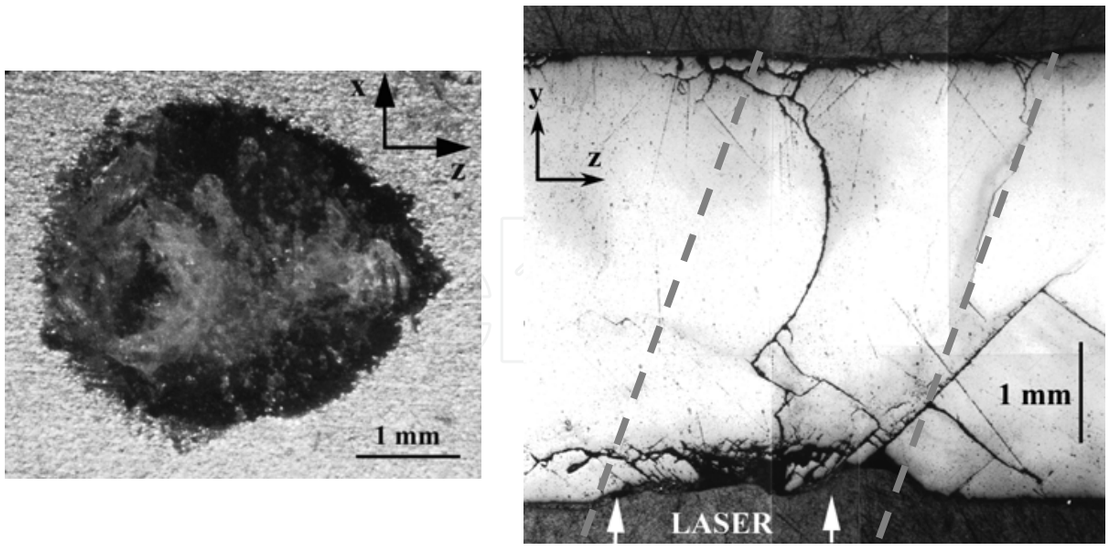

(a) **(b)**

Fig. 3. Optical micrograph of the free surface **(a)** and cross section in a *y-z* plane **(b)** of a 4.5 mm-thick quartz sample recovered after a laser shock of ~30 GPa applied onto a 2.1 mm-diameter circular spot along the *y* axis.

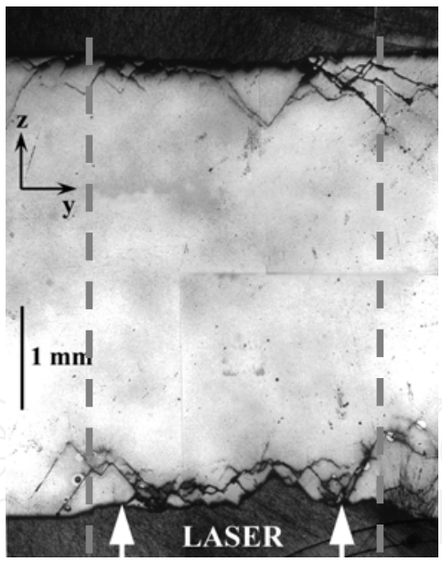

Fig. 4. Cross section in a *y-z* plane of a 4.5 mm-thick quartz sample recovered after a laser shock of ~25 GPa applied onto a 2.1 mm-diameter circular spot along the *z* axis.

decay of short laser shocks with propagation distance, the peak compressive stress rapidly attenuates down to the Hugoniot elastic limit (~6 GPa in *x*-cut quartz), so that the phenomena observed near the free surface depend essentially on the elastic response. To account for this elastic behaviour, we have implemented into *Radioss* a constitutive law based on the stiffness matrix of trigonal crystals like quartz (Royer & Dieulesaint, 1996):

$$C_{\alpha\beta} = \begin{vmatrix} C_{11} & C_{12} & C_{13} & C_{14} & 0 & 0 \\ C_{12} & C_{11} & C_{13} & -C_{14} & 0 & 0 \\ C_{13} & C_{13} & C_{33} & 0 & 0 & 0 \\ C_{14} & -C_{14} & 0 & C_{44} & 0 & 0 \\ 0 & 0 & 0 & 0 & C_{44} & C_{14} \\ 0 & 0 & 0 & 0 & C_{14} & (C_{11}-C_{12})/2 \end{vmatrix} \quad (1)$$

where subscripts α and β refer to the crystallographic directions *x,y,z* (Fig. 1) : *1* stands for *xx*, *2* for *yy*, *3* for *zz*, *4* for *yz*, *5* for *xz*, and *6* for *xy*. The *x,y,z* axes, attached to each finite element, are allowed to rotate with shock-induced motion. The stresses T_α are computed from the strains S_β according to Hooke's law, neglecting the piezoelectric contribution:

$$T_\alpha = C_{\alpha\beta} S_\beta \quad (2)$$

A simple criterion assuming instantaneous stress relaxation in the elements where the tensile stress reaches a constant threshold value has been added to handle spall fracture. As discussed elsewhere (De Rességuier et al., 2005), realistic simulations of our shock experiments, where very steep pressure pulses (with rise times of a few ns imposing a very fine mesh) propagate in large volumes, would require a great number of cells beyond our computational capabilities. Instead, we use a relatively coarse grid (~150 000 elements) which leads to an artificial spreading of the stress pulses and therefore limits the quantitative consistency of the predictions.

Fig. 5 illustrates the computed response of a 5 mm-thick quartz sample to the same laser shock as in Fig. 2, applied onto a 1.6 mm-diameter circular spot in the centre of the bottom surface, along the *x* axis of the crystal. Lateral dimensions of 10 mm have been chosen, lower than the dimensions of the real target, but enough to minimize edge effects. The distribution of longitudinal stress σ is shown at two different times. The upper part of the sample has been set 'transparent' (drawn as points) to visualize the emergence of the pulse at different depths. The threshold tensile stress for rupture has been set to 2.5 GPa in order to obtain reasonable residual damage. Actually, a lower, more realistic spall strength of 1.5 GPa (De Rességuier et al., 2003) would lead to overestimate the damage, because the duration of the stress pulse is artificially increased by the mesh coarseness. After 0.51 µs (Fig. 5a), a compressive pulse ($\sigma < 0$) has propagated from the irradiated surface through 3 mm. Its amplitude has decayed down to about 2 GPa, and the initially circular shape of the compressed zone has transformed into an elliptical shape, with a major axis at a 35° angle from the *z* axis. When that pulse reflects from the free (upper) surface, after about 0.91 µs, tensile stresses are induced in an elliptical zone (Fig. 5b). Their amplitude is too low to produce fracture inside the sample, but it is probably high enough to eject the thin gold layer (not accounted for in the simulation). Later, tension is increased by lateral waves issued from the edges of the ellipsoid, so that spallation takes place near the extremities, in the form of two penny-shaped cracks, about 170 µm below the free surface (Fig. 5c). All these results are in good agreement with the experimental observations reported above.

Fig. 6 depicts the response of a 5 mm-thick quartz sample to the same laser shock applied in the centre of the bottom surface, along the *y* axis (Fig. 6a) or the *z* axis (Fig. 6b). The reflection of the pulse from the free surface induces tensile stresses and spall damage. Again, the upper part of the sample is set 'transparent' to visualize the stress and crack distributions 200 µm below the surface. In Fig. 6a, the pulse has propagated along an

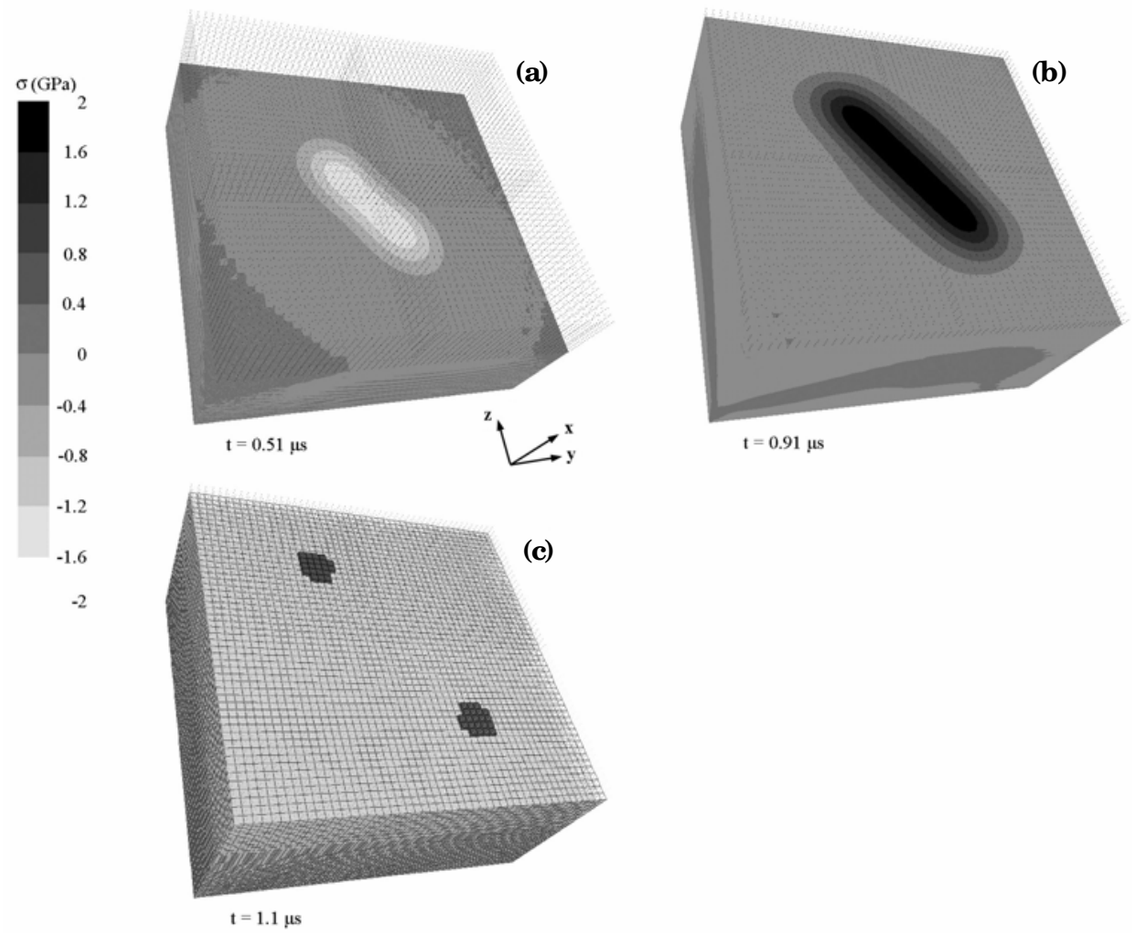

Fig. 5. Computed response of a 5 mm-thick quartz sample to a laser shock of ~42 GPa applied on a 1.6 mm-diameter spot in the bottom surface (not shown), along the x axis. The distribution of longitudinal stress is plotted 0.51 µs (a) and 0.91 µs (b) after the shot. The residual spall damage consists in two separate cracks, appearing as dark grey elements (c).

oblique direction, with an angle of about 23° from the y axis, so that damage occurs in a roughly circular (slightly 'D'-shaped) region shifted about 2 mm from the centre in the z direction. In Fig. 6b, spallation occurs in a circular zone, still in the centre of the target (i. e. above the loaded spot). Again, these predictions match the observed behaviour.

Thus, the analysis of the residual spall damage in laser shock-loaded quartz samples shows that the anisotropy of such trigonal crystals has a key influence on stress wave propagation, which strongly depends on the direction of load application versus crystal orientation. A simple elastic description involving the rigidity matrix of quartz is shown to account for those effects that were never evidenced previously.

3. Two-dimensional wave propagation in laser shock-loaded aluminium

In most laser shock experiments, the diameter of the irradiated spot is much larger than the target thickness (typically 5 times greater), which ensures conditions of uniaxial strain in the central zone near the laser axis, where edge effects do not affect the material response (e.g.

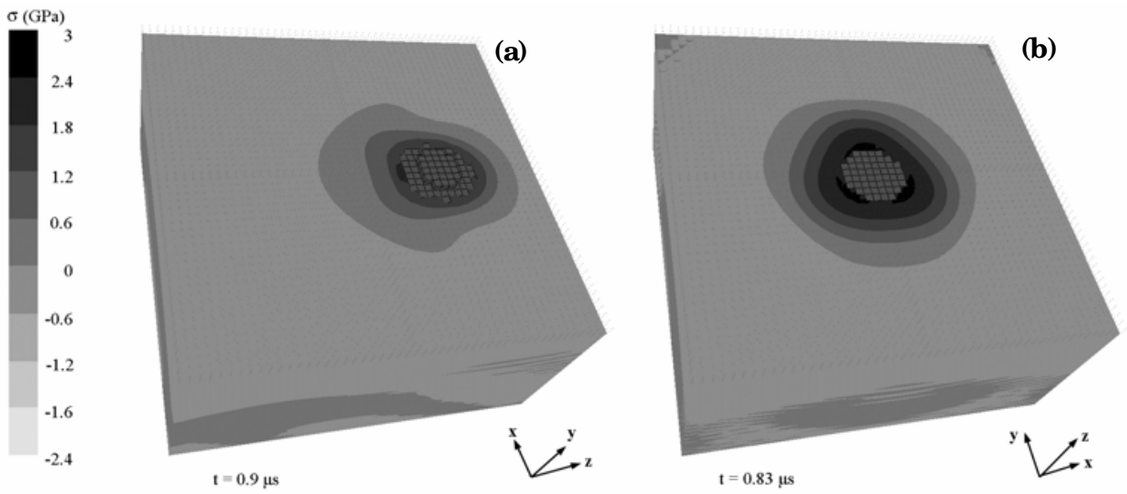

Fig. 6. Computed stress distribution in a 5 mm-thick quartz sample submitted to a laser shock of ~42 GPa applied on a 1.6 mm-diameter spot in the bottom surface (not shown), along the *y* axis **(a)** or the *z* axis **(b)**. The grey elements have been deleted after reaching the spall strength.

Boustie & Cottet, 1991; De Rességuier et al., 1997, Tollier et al., 1998). In thicker samples, such edge effects include lateral release waves issued from the periphery of the loaded area (Fig. 7), following the planar compression front and inducing a pressure decay in the transverse direction, in addition to the classical hydrodynamic attenuation of the pulse during its propagation along the symmetry axis. In such conditions, the space and time distribution of the tensile stresses induced by release waves interactions is strongly conditioned by the aspect ratio L/D between the target thickness L and the laser spot diameter D. Then, the observation of the resulting spall damage in the recovered samples coupled with 2D numerical simulations can be used to reconstitute the pressure wave propagation history (Cuq-Lelandais et al., 2009).

To illustrate this statement, we present laser shock experiments performed in the LULI, on aluminium samples of thickness 1 or 2 mm. Laser pulses of 3 ns duration and intensities ranging from 0.3 to about 30 TW/ cm² are focused on spots of diameter ranging from 1 to 4 mm. A Velocity Interferometer System for Any Reflector (VISAR) (Barker & Hollenbach, 1972) is used to measure the velocity of the free surface, in a point opposite to centre of the loaded spot. Fig. 8 shows micrographs of this free surface in 1 mm-thick samples recovered from laser shots of increasing intensity applied on spots of two different diameters corresponding to an aspect ratio of 0.25 (top) or 1 (bottom). Gradual evolution from undamaged to bulged surface is seen at low intensity, then a crater appears for higher intensities, characteristic of the ejection of a spalled layer. Unlike in quartz (see Section 2) all damaged zones are roughly circular, like the irradiated spots. For a given aspect ratio, their diameter is shown to increase with laser intensity. Fig. 9 shows cross sections of two 1 mm-thick samples (top-d and bottom-b in Fig. 8) subjected to two laser shots of similar intensity (i.e. similar shock pressure) applied on spots of different diameters. While a spalled layer has been ejected from the first target, the second one has a bulged free surface. This difference clearly illustrates the dependency of spall damage on the aspect ratio L/D.

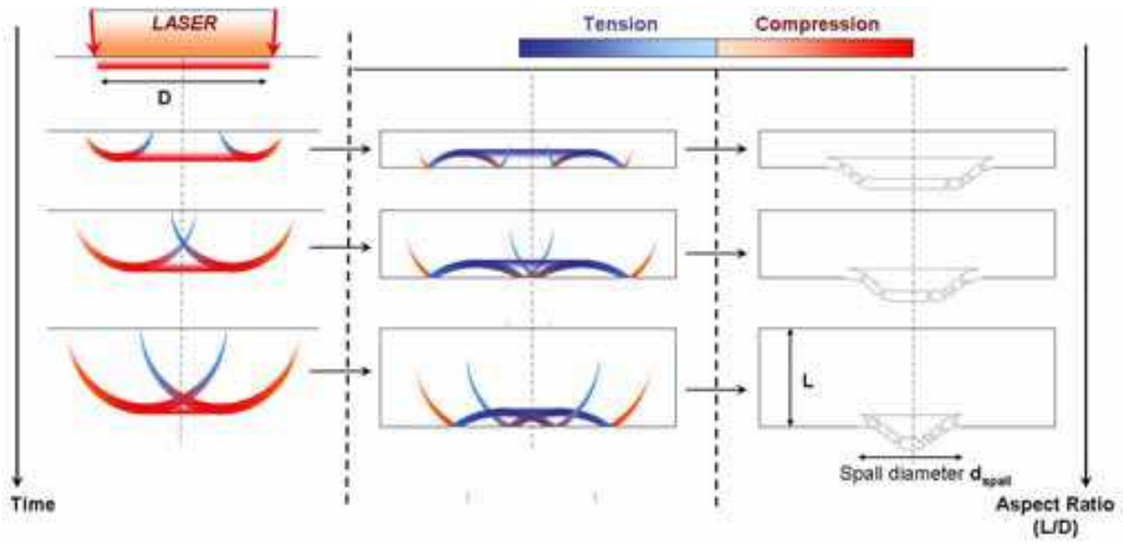

Fig. 7. Schematic description of the propagation of a laser shock of moderate intensity in samples of increasing aspect ratio, illustrating the role of edge effects in wave interactions and their consequences on the spallation process.

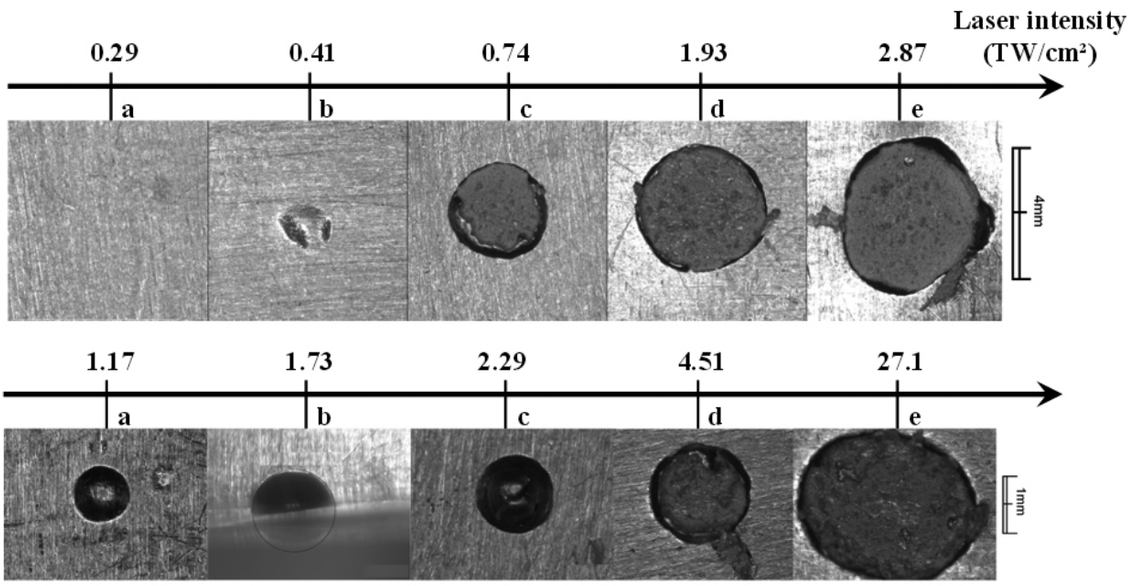

Fig. 8. Overview of the free surface in 1 mm-thick aluminium targets recovered from laser shocks of increasing intensities with two different laser spot diameters : D = 4 mm, L/D = 0.25 (top) ; D = 1 mm, L/D = 1 (bottom).

To correlate the above observations to stress wave propagation, 2D numerical simulations have been performed with the *Radioss* code. Aluminium is modelled with a Mie-Grüneisen equation of state, a Johnson-Cook constitutive law (Johnson & Cook, 1983) and a constant tensile strength to account for spall fracture. Laser shock loading is modelled with a pressure pulse applied as an input boundary condition over the irradiated spot. The temporal shape of this pressure load is inferred from 1D laser-matter interaction computations performed with the *FILM* code of the LULI (Fig. 10a). A scale factor is used to

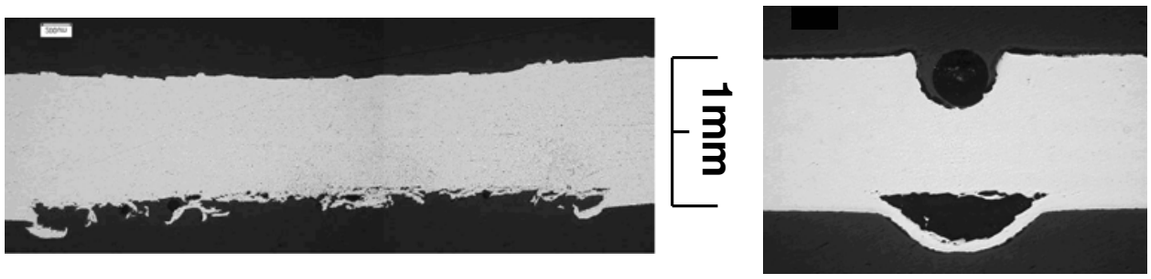

Fig. 9. Sections of 1 mm-thick aluminium samples recovered after laser shots (applied on the upper surface) of 1.9 TW/ cm² on a 4 mm-spot (left) and 1.7 TW/ cm² on a 1 mm-spot (right).

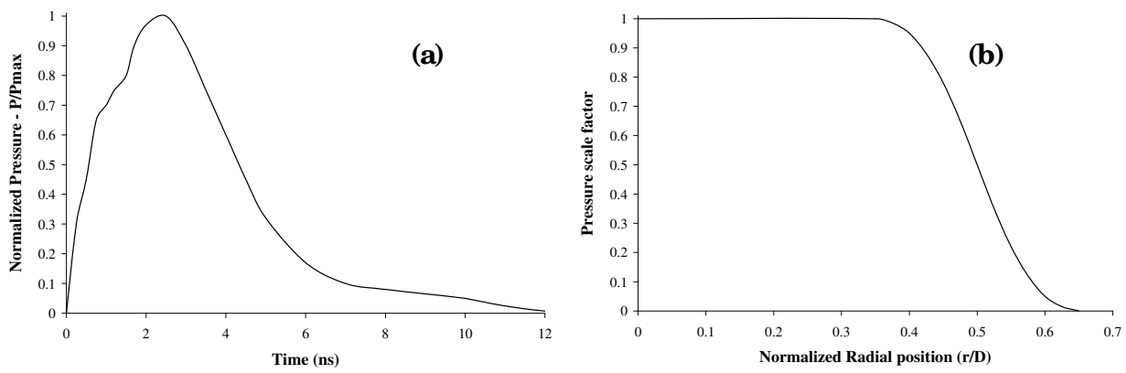

Fig. 10. Temporal **(a)** and spatial **(b)** shapes of the pressure distribution imposed as an input boundary condition over the loaded surface in the computations.

account for the radial decrease of loading pressure with laser energy in the peripheral region of the irradiated area (Fig. 10b). Fig. 11 shows the computed distribution of axial stress at different times for two different geometrical configurations, with a 50 GPa peak loading pressure representative of a ~2 TW/ cm² laser shot. A planar shock front parallel to the irradiated surface propagates along the laser axis (Fig. 11-t1) while spherical waves are generated from the edges of the loaded spot (Fig. 11-t2), both outward (compression waves) and inward (release waves). The interaction of these lateral release waves with the planar unloading wave following the laser shock creates tension zones just behind the main compression front. For the higher aspect ratio, these lateral waves meet on the symmetry axis where their crossing generates a new tension pulse that propagates along this axis (Fig. 11b-t3 and t4).

Finally, the reflection of the incident pressure pulse from the free surface produces tensile loading in a planar region close to that surface, as classically occurring in 1D geometry. Thus, the spatial and temporal distribution of dynamic tension results from complex interactions between many waves. As soon as it reaches locally the threshold tensile strength of the material, damage occurs in the form of element deletion accompanied by instantaneous stress relaxation (Fig. 11-t5). Although the pressure load is the same for both cases, the resulting damage differs, either bulging or ejection of a spalled layer (Fig. 11-t7), depending on the aspect ratio. These predictions are consistent with the experimental results presented above (Fig. 9).

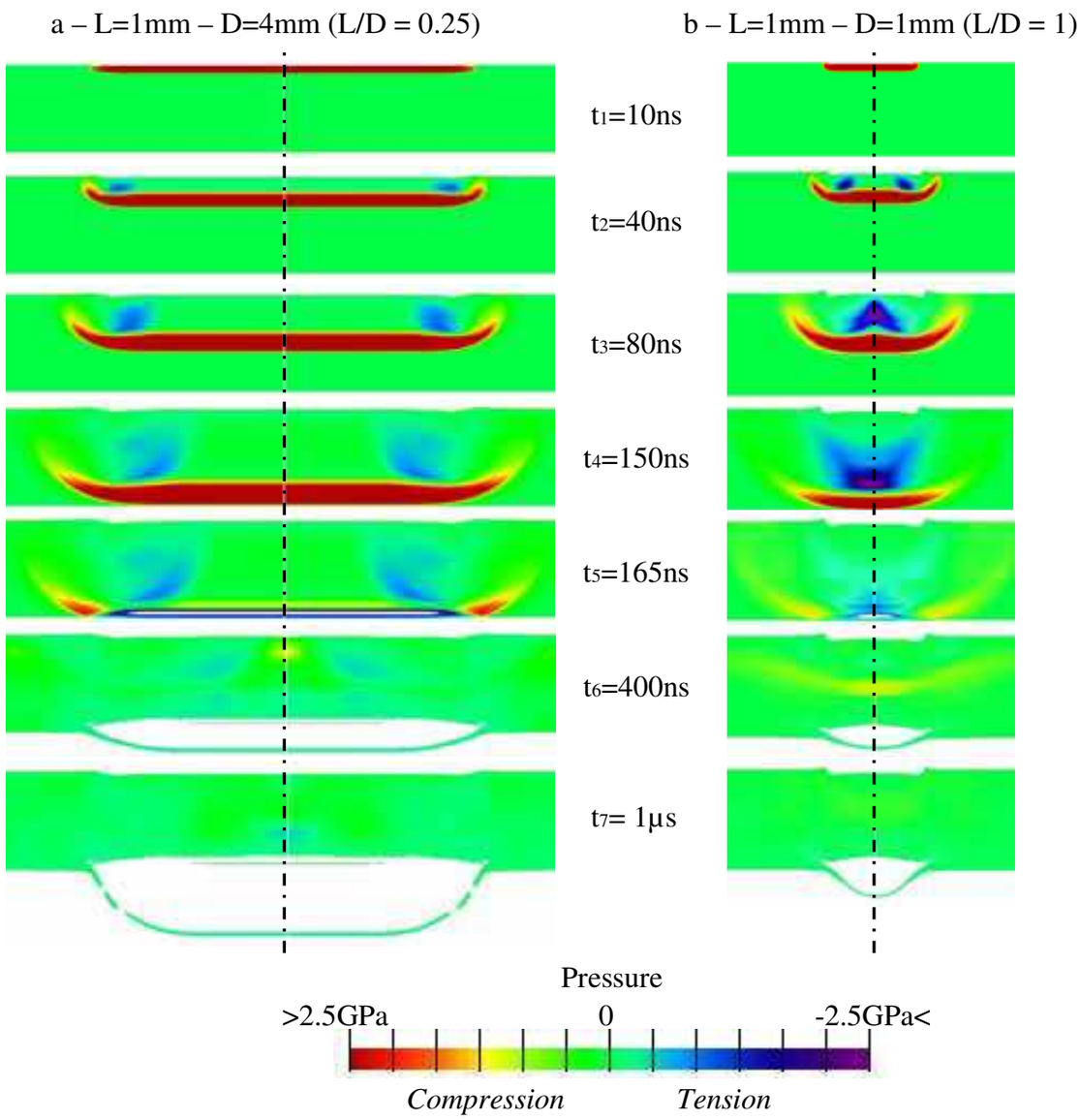

Fig. 11. Computed distribution of axial stress at successive times in 1 mm-thick aluminium targets subjected to a 50 GPa laser shock with aspect ratios L/D = 0.25 **(a)** and L/D = 1 **(b)**.

Contributions of 2D effects can also be evidenced in the free surface velocity profiles measured on the central axis. Fig. 12 shows a comparison between experimental VISAR signals recorded behind 1 mm-thick samples subjected to 50 GPa laser shocks applied on two spots of different diameters (solid lines) and the computed profiles resulting from the 2D simulations above (dotted lines). All curves start with a sharp acceleration upon shock breakout, followed by a progressive deceleration due to the reflection of the unloading wave, interrupted by oscillations characteristic of the spall process. Based on an acoustic approximation, the dynamic tensile strength of the material can be estimated from the so-called velocity pullback (Antoun et al., 2002). This pullback (Δu in Fig. 12) is 350 m/ s in both records, which leads to a spall strength of 2.5 GPa. A good overall agreement is found

between the measured and calculated velocity profiles, except for the final oscillations, corresponding to wave reverberation through the spalled layer, much too strong in the computations. This discrepancy points out the limitations of the very simple failure criterion, not accounting for the damage dynamics. Peak velocity is found to depend strongly on the aspect ratio, since it is almost twice higher for the 4 mm-spot than for the 1 mm-spot. This is due to the additional attenuation of the pressure pulse by the lateral release waves when they reach the central zone before the shock breaks up at the free surface (see Fig. 7). A 1D simulation has been performed with the same pressure load and target thickness. It is found to match exactly the 2D simulation for the smaller aspect ratio (L/D = 0.25), which shows that edge effects have not affected wave propagation along the central axis in that case.

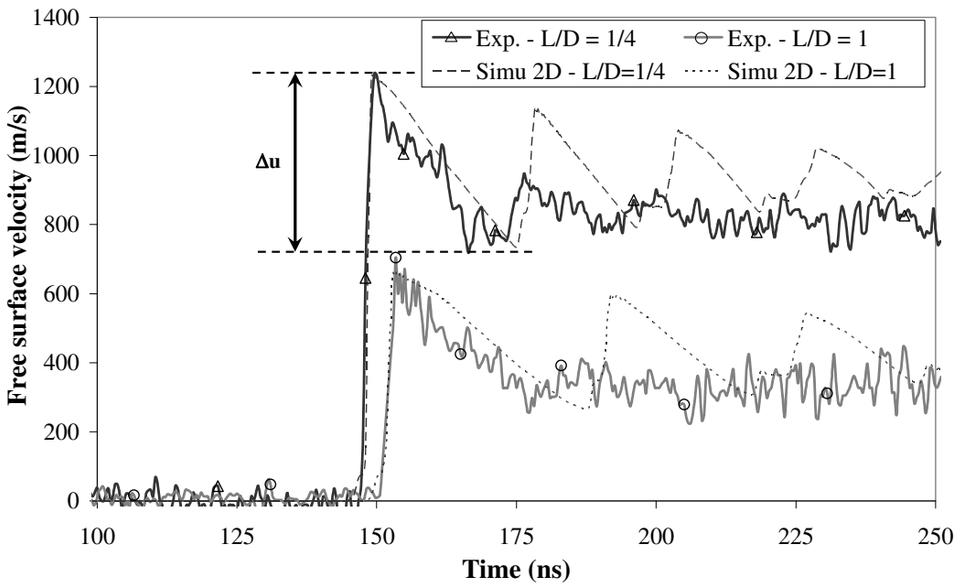

Fig. 12. Comparison of the velocity profiles measured (solid lines) and calculated (dotted lines) at the free surface of 1 mm-thick aluminium samples subjected to laser shocks of 50 GPa applied on spots of diameter 4 mm (L/D = 0.25) or 1 mm (L/D = 1).

The diameter of the spalled zones measured in the free surfaces shown in Fig. 8 is plotted in Fig. 13 for various loading pressures and both aspect ratios, compared to the results of 2D simulations. A good consistency is obtained between experiments and calculations. A zero diameter means that no spallation could be observed. In the computations, this absence of spall damage is represented by the vertical dashed line. In a 1D geometry, one would expect a spalled zone of same diameter as the laser spot. This is observed for loading pressures of 40 GPa with L/D = 1 (D = 1 mm), and about 60 GPa with L/D = 0.25 (D = 4 mm). Above those pressure values, the spalled zone is larger than the loaded spot (e.g. Fig. 9b), because of the effects of the spherical compressive waves propagating outward from the edges of this spot (see Fig. 7). Below those values, the diameter of the spalled zone decreases with loading pressure, because of the attenuation of the compressive pulse by the lateral release waves. Thus, simple examination of the free surface of spalled samples provides indications about the shock pressure applied onto the opposite surface and the subsequent stress wave propagation.

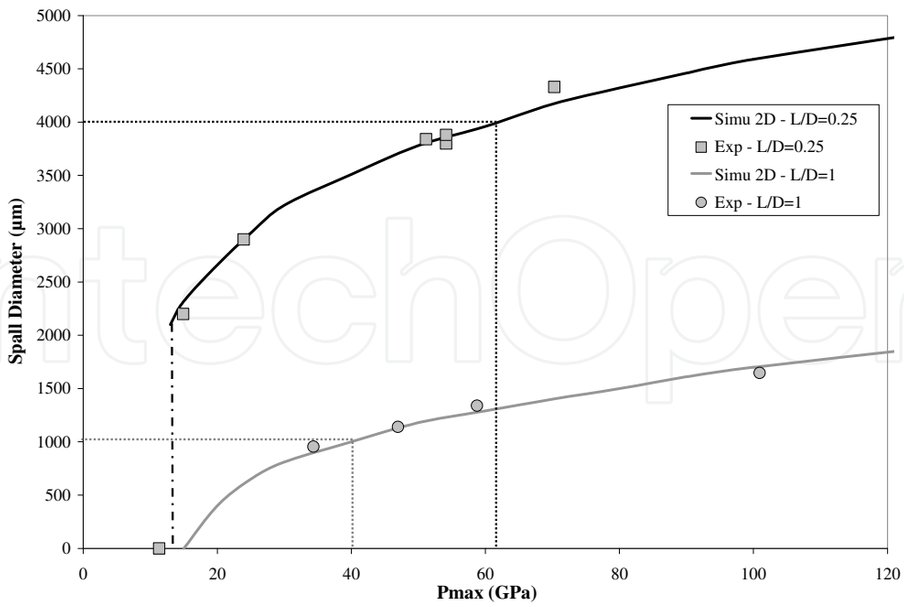

Fig. 13. Comparison of the measured and calculated diameters of the spalled zone in the free surface of 1 mm-thick samples after laser shocks of increasing intensity applied on spots of diameter 4 mm (L/D = 0.25) or 1 mm (L/D = 1).

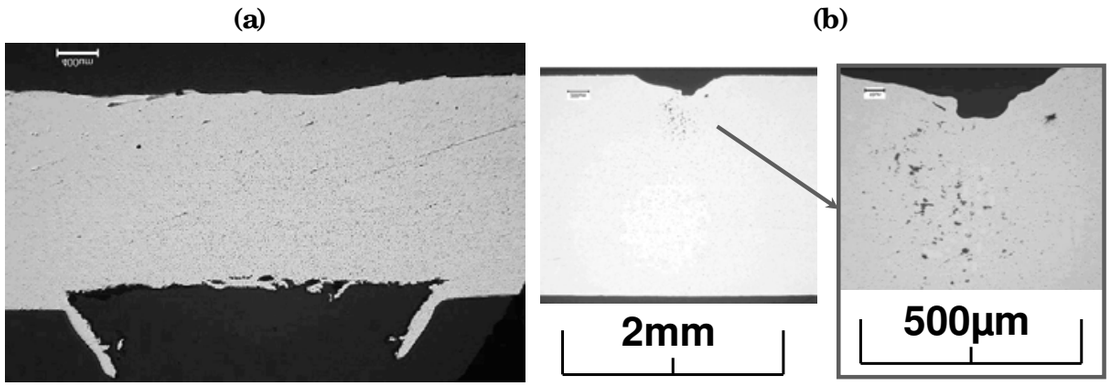

Fig. 14. Cross sections of 2 mm-thick aluminium samples recovered after laser shocks of about 2 TW/ cm² applied on spots of diameter 4 mm **(a)** or 1 mm **(b)** in the upper surface.

Finally, 2D effects can lead to damage mechanisms different from spallation (Boustie et al., 2007). Fig. 14 shows cross sections of 2 mm-thick aluminium targets subjected to laser shocks of same intensity applied on spots of different diameters. The first sample (Fig. 14a), of smaller aspect ratio (L/D = 0.5), is typical of the ejection of a planar spalled layer. The second one (L/D = 2) presents no sign of spall fracture near the free surface, but damage appears in the form of pores down to about 500 µm beneath the loaded zone (Fig. 14b). Such damage results from the interaction of the lateral release waves issued from the edges of the laser spot (see Fig. 11b). When they meet in the central zone near the symmetry axis, their crossing produces tensile stresses higher than the dynamic strength of the metal, which causes void nucleation and growth. Meanwhile, the compressive pulse emerging at the free surface after both axial and lateral decay is too low to produce spallation.

Overall, like in the previous section, post-shock analysis of the residual damage in laser shock-loaded samples combined with numerical simulations can be used to investigate wave propagation, especially the complex 2D effects that become prominent (even in an isotropic solid like aluminium) as soon as the diameter of the loaded surface is of the same order as the sample thickness.

4. Phase transformation and wave propagation in laser shock-loaded iron

When shocked above 13 GPa, iron undergoes a polymorphic (solid-solid) transformation from body-centered-cubic (α) to hexagonal-close-packed (ε) structure. This transition was first inferred from wave profile measurements several decades ago (Minshall, 1955; Bancroft et al., 1956), then corroborated under quasi-static compression (Jamieson & Lawson, 1962). Although it has been reported that tiny quantities of ε phase could be quenched to ambient pressure upon release following ultra-short, fs-duration laser-driven shocks (Sano et al., 2003), the transformation is essentially reversible, so the ε structure can only be detected during the time of pressure application, which makes direct identifications challenging (Kalantar et al., 2005; Hawreliak et al., 2006). One indirect way to characterize this phase change under shock conditions is to study the subsequent formation of double wave structures from initially steep shock fronts (Barker & Hollenbach, 1974; Duvall & Graham, 1977; Boettger & Wallace, 1997). Another one is to analyze the residual distribution of specific micro-twins following the excursion into the high pressure phase (Smith, 1958; Johnson et al., 1962) and leading to a significant increase in the material residual hardness. Here, we use spall fracture as a third indirect approach to study this phase transition and its effects on wave propagation in laser shock-loaded iron.

Again, the experiments have been performed in the LULI. A pulsed laser beam of 1.06 µm-wavelength, 4.5 ns-duration, and ~1000 J-energy is focused onto a 2.8 mm-diameter spot on pure polycrystalline iron foils of thicknesses ranging from 150 µm to 520 µm, set in a vacuum chamber to avoid laser breakdown in air. The resulting irradiation at about 5×10^{12} W/ cm^2 produces the vaporization of a thin layer of material whose expansion induces by reaction a compressive pulse into the solid target. The amplitude and shape of this pressure pulse are inferred from 1D computations of laser-matter interaction with the code *FILM* of the LULI. The resulting load consists of a sharp compression within about 1 ns to a peak pressure of ~130 GPa followed by slower unloading in about 8 ns. Like in Section 3, a VISAR interferometer is used to measure the velocity of the opposite free surface. The recovered samples are embedded in a resin, sectioned through a plane containing the laser axis, etched with a Nital solution to reveal grain boundaries and defects, and observed in optical microscopy.

The 150 µm-thick target was fully pierced by the laser shot, so that nothing could be recovered from the shocked zone. The thicker samples remained attached to the target holder. Fig. 15 shows cross sections of shock-loaded samples of initial thicknesses 520 µm (a), 400 µm (b) and 250 µm (c). The laser shock has been applied onto the lower surface, and its reflection from the upper free surface has lead to the ejection of a ~90 to 110 µm-thick spalled layer. In addition, high shear stresses induced in the periphery of the loaded zone have cut out the 250 µm-thick foil, so the cross section is split into three parts.

Higher magnification micrographs of two of those cross sections after etching are presented in Fig. 16, showing detailed views below the spall craters (upper surfaces). In the two thicker samples, spallation occurs in the form of straight cracks, both intra- and inter-

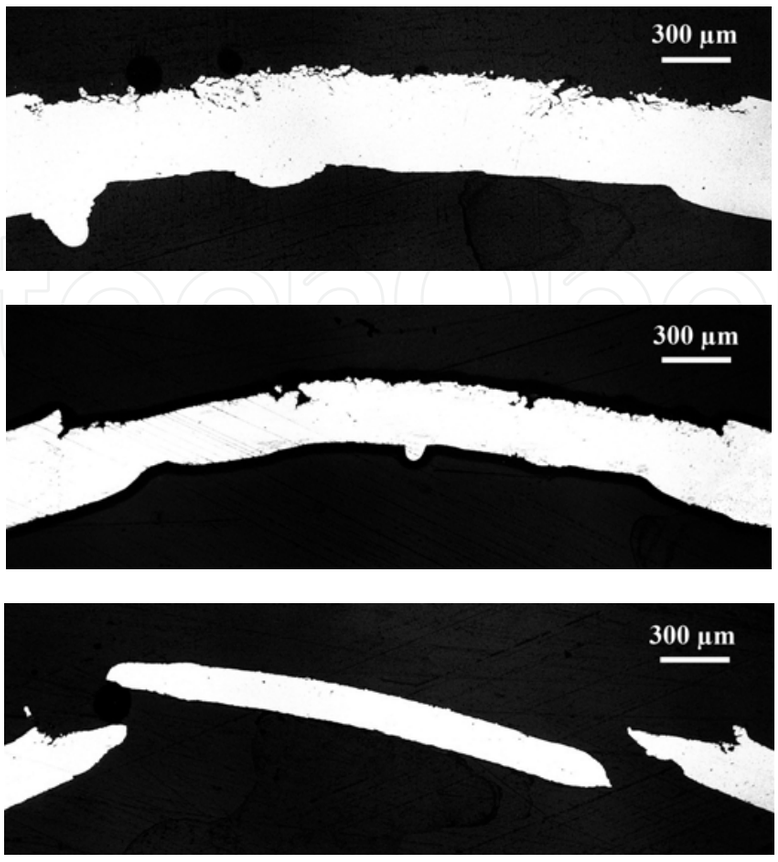

Fig. 15. Cross sections in iron samples of initial thickness 520 µm **(a)**, 400 µm **(b)**, and 250 µm **(c)**, recovered after laser shocks of about 130 GPa applied onto the bottom surface. The ejection of a spalled layer results in a ~90 to 110 µm-deep crater in the upper surface.

granular, consistent with the brittle fracture behaviour of iron at high strain rates (Zurek & Meyers, 1996), distributed over a depth of several tens of µm (Fig. 16a). In the 250 µm-thick sample, the spall plane is remarkably smooth (Fig. 15c and 16b). Such "smooth spall", already reported under explosive and impact loading, is interpreted as a sign that fracture took place after completion of the α–ε–α cycle (Ivanov & Novikov, 1986; Novikov et al., 1994; Voltz et al., 2006). It is usually attributed to the formation of a rarefaction shock resulting from the steepening of the release wave upon reverse transformation back to the α phase, which produces a drop in density and an increase in sound speed. As mentioned earlier, the change to the ε phase should also result in the formation of specific micro-twins. Actually, such micro-twins can be seen in the first grains at the bottom of Fig. 16a (400 µm-thick sample), suggesting that significant amount of ε-phase has been formed up to about 100 µm away from the spall crater, while extensive twinning is observed up to the spall plane in Fig. 16b (250 µm-thick sample). This confirms that the spalling region has remained in the α-phase in the thicker sample (rough fracture surface) while it has undergone the α–ε–α cycle before fracture in the thinner one (smooth fracture surface). Such difference provides information on the decay of the laser driven pressure pulse during its propagation from the irradiated surface, since it indicates that peak pressure has remained higher than the 13 GPa-threshold required for the phase transformation over a propagation distance of about 300 µm.

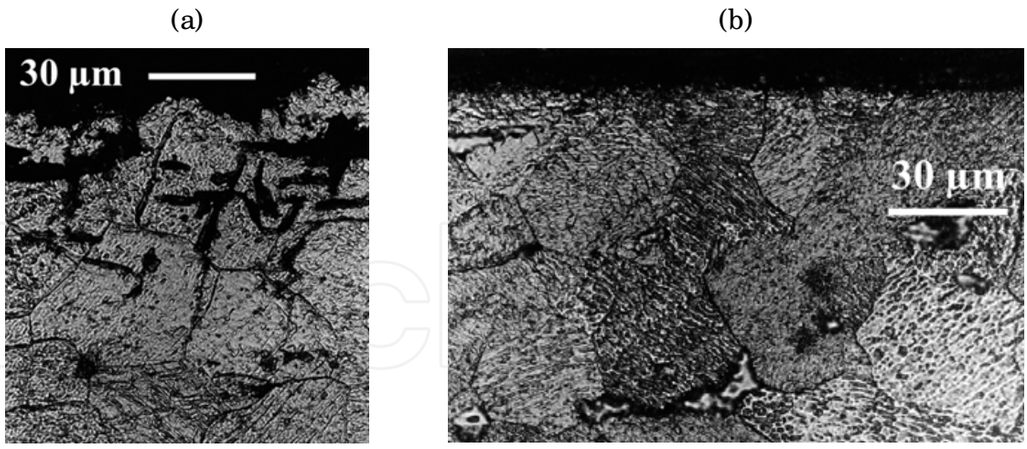

Fig. 16. Detailed views of the spall craters (upper surfaces) in cross sections of laser shock-loaded iron samples of initial thickness 400 µm **(a)** and 250 µm **(b)** after etching. The 250 µm-thick sample exhibits a remarkably smooth fracture surface, as well as a dense distribution of micro-twins up to that surface.

VISAR records of the free surface velocity are shown in Fig. 17. A vertical shift of -200 m/ s has been added between the shots for clarity. They all show an elastic precursor followed by a slower plastic front which does not split into the two-wave structure usually observed over larger propagation distances. The peak free surface velocity drops rapidly while the target thickness increases from 150 µm to 250 µm, then it decreases slowly with propagation distance. As already discussed in Section 3, fracture-induced stress relaxation gives rise to compressive waves that propagate from the cracks and produce a re-acceleration of the free surface called the spall pulse (Antoun et al., 2002). Thereafter, wave reverberation within the spalled layers generates damping oscillations in the velocity profiles. These profiles are compared to the results of 1D simulations with the *SHYLAC* code, involving a two-phase equation of state with a description of the kinetics of the phase change (De Rességuier & Hallouin, 2001), a constitutive law accounting for time-dependent twinning (De Rességuier & Hallouin, 1998), and a simple spall criterion assuming instantaneous rupture and subsequent relaxation as soon as the tensile stress reaches a threshold value. This comparison, which has been discussed in details elsewhere (De Rességuier & Hallouin, 2008), shows a good overall consistency. According to the model predictions, the decay of the pressure pulse should yield to full transition from α to ε iron in the first ~200 µm below the loaded surface, then the fraction of ε phase should decrease from 1 to 0 through the next ~200 µm-thick layer. Hence the tensile stresses leading to spall fracture upon reflection of the compressive pulse from the free surface would be induced in a region of untransformed α iron in the 520 µm-thick sample, in a material having undergone very little (less than 8 %) α–ε phase transformation in the 400 µm-thick sample, and in a zone which was almost fully transformed in the two thinner targets. This is fully consistent with the difference in fracture surface morphology reported above.

Finally, a smooth fracture surface similar to that observed in the 250 µm-thick sample can be seen in the left part of the spall crater in Fig. 15b, in the 400 µm-thick sample. As stated above, the α–ε phase transition should have propagated only up to about 100 µm beneath the spall plane (Fig. 16a). However, some hotter spot in the laser beam may have lead to a

somewhat inhomogeneous spatial distribution of the loading pressure applied onto the irradiated surface, so that the depth of the transformed region may have reached the spall plane in this left part of the cross section, which would account for the smooth spall.

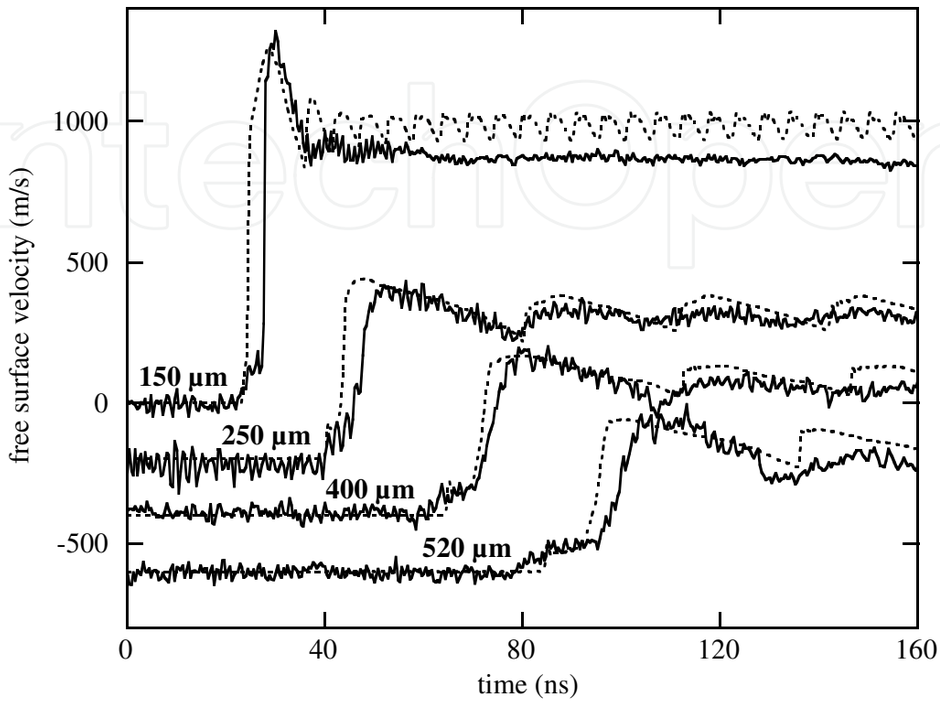

Fig. 17. Solid lines are free surface velocity profiles measured in iron samples of different thicknesses (bold numbers) subjected to laser shocks of about 130 GPa. For clarity, some records have been shifted vertically (offsets of -200 m/ s, -400 m/ s and -600 m/ s have been subtracted from the velocity for thicknesses of 250 µm, 400 µm and 520 µm, respectively. Dotted lines result from computer simulations of the experiments.

Thus, the change in fracture surface morphology observed in iron samples of increasing thicknesses recovered after laser shock-induced spallation provides a signature of the α–ε phase transformation occurring in this metal, which can be used to infer the decay of shock pressure with propagation distance, as well as the spatial distribution of the pressure applied onto the loaded surface.

5. Conclusion

Dynamic fracture in shock-loaded materials is governed by the propagation, reflection and interactions of stress waves. Post-shock analyses of the residual damage observed in samples recovered from laser shock experiments, less destructive than more conventional techniques, can provide valuable insight into key aspects of wave propagation prior to fracture, such as the effects of structural anisotropy, the role of lateral waves associated to edge effects, or the influence of polymorphic phase transformations on the response to shock loading. Such observations can be based on very simple techniques like optical microscopy. Still, their interpretation should be comforted by time-resolved measurements

and numerical simulations since the phenomenology leading to the final damage may include several complex, coupled processes.

6. References

Antoun, T.; Seaman, L.; Curran, D.R.; Kanel, G.I.; Razorenov, S.V. & Utkin, A.V. (2002). *Spall Fracture*, Ed. Springer, ISBN 0-387-95500-3

Bancroft, D.; Peterson, E.L. & Minshall, S. (1956). Polymorphism of iron at high pressure, *J Appl. Phys.* 27(3), pp. 291-298

Barker, L.M. & Hollenbach, R.E. (1972). Laser interferometer for measuring high velocities of any reflecting surface, *J Appl. Phys.* 43, pp. 4669-4675

Barker, L.M. & Hollenbach, R.E. (1974). Shock wave study of the α–ε phase transition in iron, *J Appl. Phys.* 45, pp. 4872-4887

Boettger, J.C. & Wallace, D.C. (1997). Metastability and dynamics of the shock-induced phase transition in iron, *Physical Review B* 55(5), pp. 2840-2849

Boustie, M. & Cottet, F. (1991). Experimental and numerical study of laser induced spallation into aluminum and copper targets, *J Appl. Phys.* 69, pp. 7533–7538

Boustie, M.; Cuq-Lelandais, J.P.; Bolis, C.; Berthe, L.; Barradas, S.; Arrigoni, M.; De Rességuier, T. & Jeandin, M. (2007). Study of damage phenomena induced by 2D effects into materials under laser driven shocks, *J Phys. D* 40, pp. 7103-7108

Cuq-Lelandais, J.P.; Boustie, M.; Berthe, L.; Combis, P.; Sollier, A.; De Rességuier, T.; Lescoute, E.; Gay, E.; Soulard, L. & Bontaz, J. (2009). Two-dimensional investigation of laser shock induced spallation in sub-picosecond regime, Proceedings of the 9th DYMAT Conference, Brussels, Belgium, September 2009, EDP Sciences, pp. 625-631

De Rességuier, T. & Cottet, F. (1995). Experimental and numerical study of laser induced spallation in glass, *J Appl. Phys.* 77(8), pp. 3756-3761

De Rességuier, T.; Couturier, S., David, J. & Niérat, G. (1997). Spallation of metals subjected to intense laser shocks, *J Appl. Phys.* 82(5), pp. 2617-2623

De Rességuier, T. & Hallouin, M. (1998). Stress relaxation and precursor decay in laser shock-loaded iron, *J Appl. Phys.* 84(4), pp. 1932-1938

De Rességuier, T. & Hallouin, M. (2001). Interaction of two laser shocks inside iron samples, *J Appl. Phys.* 90(9), pp. 4377-4384

De Rességuier, T.; Berterretche, P. & Hallouin, M. (2005). Influence of quartz anisotropy on shock propagation and spall damage, *Int. J of Impact Engineering* 31(5), pp. 545-557

De Rességuier, T. & Hallouin, M. (2008). Effects of the α–ε phase transition on wave propagation and spallation in laser shock-loaded iron, *Phys. Rev. B* 77(17), 174107

Duvall, G.E. & Graham, R.A. (1977). Phase transition under shock wave loading, *Rev. Mod. Phys.* 49, pp. 523-579

Hawreliak, J; Colvin, J.D.; Eggert, J.H.; Kalantar, D.H.; Lorenzana, H.E.; Stölken, J.S.; Davies, H.M.; Germann, T.C.; Holian, B.L.; Kadau, K.; Lomdahl, P.S.; Higginbotham, A.; Rosolankova, K.; Sheppard, J. & Wark, J.S. (2006). An analysis of the X-ray diffraction signal for the α–ε transition in shock-compressed iron: simulation and experiment, *Phys. Rev. B* 74, 184107

Ivanov, A.G. & Novikov, S.A. (1986). Rarefaction shock waves in iron from explosive loading, *Comb. Expl. Shock Waves* 22(3), pp. 343-350

Jamieson, J.C. & Lawson, A.W. (1962). X-ray diffraction studies in the 100 kbar pressure range, *J Appl. Phys.* 33(3), pp. 776-780

Johnson, G.R. and Cook, W.H. (1983). A constitutive model and data for metals subjected to large strains, high strain rates and high temperatures, Proceedings of the 7th Int. Symp. on Ballistics, La Hague, pp. 541-547

Johnson, P.C.; Stein, B.A. & Davis, R.S. (1962). Temperature dependence of shock-induced phase transformation in iron, *J Appl. Phys.* 33, pp. 557-562

Kalantar, D.H.; Belak, J.F.; Collins, G.W.; Colvin, J.D.; Davies, H.M.; Eggert, J.H.; Germann, T.C.; Hawreliak, J.; Holian, B.L.; Kadau, K.; Lomdahl, P.S.; Lorenzana, H.E.; Meyers, M.A.; Rosolankova, K.; Schneider, M.S.; Sheppard, J.; Stölken, J.S. & Wark, J.S., Direct observation of the α–ε transition in shock-compressed iron via nanosecond X-ray diffraction (2005). *Phys. Rev. Lett.* 95(7), 075502

Li X.-Z., Nakano M., Yamauchi Y., Kishida K. and Tanaka K.A. (1998). Microcracks, spall and fracture in glass : a study using short pulsed laser shock waves, *J Appl. Phys.* 83(7), pp. 3583-3594

Minshall, S. (1955). Investigation of polymorphic transition in iron at 130 kbar, *Phys. Rev.* 98(3), p. 271

Novikov, S.A.; Pogorelov, A.P. & Sinitsyna, L.M. (1994). The formation of smooth spalls in steel during the interaction of glancing detonation waves, *Comb. Expl. Shock Waves* 30(4), pp. 537-539

Royer, D. & Dieulesaint, F. (1996). *Ondes élastiques dans les solides (Tome 1, Propagation libre et guidée)*, ed. Masson, Paris

Sano, T.; Mori, H.; Ohmura, E. & Miyamoto, I. (2003). Femtosecond laser quenching of the ε phase of iron, *Appl. Phys. Lett.* 83(17), pp. 3498-3500

Smith, C.S. (1958). Metallographic studies of metals after explosive shock, Trans. Metall. Soc. AIME 212, pp. 574-589

Tollier, L.; Fabbro, R. & Bartnicki, E. (1998). Study of the laser-driven spallation process by the VISAR interferometry technique II: experiment and simulation of the spallation process, *J Appl. Phys.* 83(3), pp. 1231-1237

Voltz, C.; Buy, F. & Roy, G. (2006). Iron damage and spalling behavior below and above shock-induced α–ε phase transition *Shock Compression of Condensed Matter*, CP845, Proceedings of APS Shock Conference, August 2005, Baltimore, USA, pp. 678-681

Zurek, A.K. & Meyers, M.A. (1996). Microstructural aspects of dynamic failure, in *High Pressure Shock Compression of Solids II*, eds. L. Davison, D.E. Grady and M. Shahinpoor, Springer, New York, pp. 25-70

Wave Propagation in Materials for Modern Applications

Edited by Andrey Petrin

ISBN 978-953-7619-65-7
Hard cover, 526 pages
Publisher InTech
Published online 01, January, 2010
Published in print edition January, 2010

In the recent decades, there has been a growing interest in micro- and nanotechnology. The advances in nanotechnology give rise to new applications and new types of materials with unique electromagnetic and mechanical properties. This book is devoted to the modern methods in electrodynamics and acoustics, which have been developed to describe wave propagation in these modern materials and nanodevices. The book consists of original works of leading scientists in the field of wave propagation who produced new theoretical and experimental methods in the research field and obtained new and important results. The first part of the book consists of chapters with general mathematical methods and approaches to the problem of wave propagation. A special attention is attracted to the advanced numerical methods fruitfully applied in the field of wave propagation. The second part of the book is devoted to the problems of wave propagation in newly developed metamaterials, micro- and nanostructures and porous media. In this part the interested reader will find important and fundamental results on electromagnetic wave propagation in media with negative refraction index and electromagnetic imaging in devices based on the materials. The third part of the book is devoted to the problems of wave propagation in elastic and piezoelectric media. In the fourth part, the works on the problems of wave propagation in plasma are collected. The fifth, sixth and seventh parts are devoted to the problems of wave propagation in media with chemical reactions, in nonlinear and disperse media, respectively. And finally, in the eighth part of the book some experimental methods in wave propagations are considered. It is necessary to emphasize that this book is not a textbook. It is important that the results combined in it are taken “from the desks of researchers“. Therefore, I am sure that in this book the interested and actively working readers (scientists, engineers and students) will find many interesting results and new ideas.

University Campus STeP Ri
Slavka Krautzeka 83/A
51000 Rijeka, Croatia
Phone: +385 (51) 770 447
Fax: +385 (51) 686 166
www.intechopen.com

Unit 405, Office Block, Hotel Equatorial Shanghai
No.65, Yan An Road (West), Shanghai, 200040, China
中国上海市延安西路65号上海国际贵都大饭店办公楼405单元
Phone: +86-21-62489820
Fax: +86-21-62489821

IntechOpen

IntechOpen